Calibration and evaluation of CCD spectroradiometers for airborne measurements of spectral actinic flux densities

Birger Bohn[1] and Insa Lohse[1,2]

[1]Institut für Energie- und Klimaforschung, IEK-8: Troposphäre, Forschungszentrum Jülich GmbH, 52428 Jülich, Germany
[2]Deutscher Wetterdienst, BTZ-Langen, 63225 Langen, Germany

Correspondence to: B. Bohn (b.bohn@fz-juelich.de)

Abstract. The properties and performance of CCD array spectroradiometers for the measurement of atmospheric spectral actinic flux densities and photolysis frequencies were investigated. These instruments are widely used in atmospheric research and are suitable for aircraft applications because of high time resolutions and high sensitivities in the UV range. The laboratory characterization included instrument-specific properties like wavelength accuracy, dark signals, dark noise and signal-to-noise

5 ratios. Spectral sensitivities were derived from measurements with spectral irradiance standards. The calibration procedure is described in detail and a straightforward method to minimize the influence of stray light on spectral sensitivities is introduced. Detection limits around $1 \times 10^{10} \mathrm{cm}^{-2}\mathrm{s}^{-1}\mathrm{nm}^{-1}$ were derived for spectral actinic flux densities in a 300 nm range (1 s integration time). As a prerequisite for the determination of stray light under field conditions, atmospheric cutoff wavelengths were defined using radiative transfer calculations as a function of solar zenith angles and ozone columns. The recommended analysis

10 of field data relies on these cutoff wavelengths and is also described in detail taking data from a research flight as an example. An evaluation of field data was performed by ground-based comparisons with a double-monochromator reference spectroradiometer. Spectral actinic flux densities were compared as well as photolysis frequencies $j(\mathrm{NO}_2)$ and $j(\mathrm{O}^1\mathrm{D})$, representing UV-A and UV-B ranges, respectively. The spectra expectedly revealed an increased daytime level of residual noise below atmospheric cutoff wavelengths that is caused by stray light. The influence of instrument noise and stray light induced noise

15 was found to be insignificant for $j(\mathrm{NO}_2)$ and rather limited for $j(\mathrm{O}^1\mathrm{D})$, resulting in estimated detection limits of $5 \times 10^{-7}\mathrm{s}^{-1}$ and $1 \times 10^{-7}\mathrm{s}^{-1}$, respectively. For $j(\mathrm{O}^1\mathrm{D})$ the detection limit could be further reduced by setting spectral actinic flux densities below cutoff wavelengths to zero. The accuracies of photolysis frequencies were determined from linear regressions with reference instrument data. The agreement was typically within ±5%. Optical receiver aspects were widely excluded in this work and will be treated in a separate paper in particular with regard to airborne applications. Overall, the investigated instruments

20 are clearly suitable for high quality photolysis frequency measurements with high time resolution as required for airborne applications. An example of data from a flight on the research aircraft HALO is presented.

1 Introduction

Solar actinic radiation is the driving force of atmospheric photochemistry because it produces short-lived reactive radicals in photolysis processes. Photolysis frequencies are first-order rate constants that quantify the corresponding loss rate of photoliz-

able compounds in the gas phase. Likewise they determine the primary production rate of the often highly reactive photolysis products like $O(^1D)$, $O(^3P)$ or OH radicals. Photolysis frequencies are therefore essential parameters for a quantitative understanding of atmospheric photochemistry.

Taking formation of $O(^1D)$ in the photolysis of ozone as an example,

$$O_3 + h\nu(\lambda \leq 340 \text{ nm}) \longrightarrow O_2 + O(^1D) \tag{R1}$$

the corresponding photolysis frequency $j(O^1D)$ is defined by:

$$\frac{d[O(^1D)]}{dt} = j(O^1D)[O_3] \tag{1}$$

Species in square brackets in Eq. 1 denote gas-phase number concentrations. The photolysis frequency $j(O^1D)$ is of particular importance because in the presence of water vapour the electronically excited $O(^1D)$ can form OH radicals, the primary atmospheric oxidant:

$$O(^1D) + H_2O \longrightarrow 2\,OH \tag{R2}$$

The connection between the chemical rate constant $j(O^1D)$ and the local solar radiation field is given via the spectral actinic photon flux density F_λ:

$$j(O^1D) = \int F_\lambda \times \sigma_{O_3} \times \phi_{O(^1D)}\, d\lambda \tag{2}$$

In this equation σ_{O_3} and $\phi_{O(^1D)}$ are molecular parameters of O_3, namely the absorption cross sections of the precursor molecule and the quantum yields of the photo-product $O(^1D)$, respectively, which confine the process mainly in the UV-B range.

Other photolysis frequencies can be determined similarly by inserting the respective molecular parameters. For example, in the case of the mainly UV-A driven NO_2 photolysis:

$$NO_2 + h\nu(\lambda \leq 420 \text{ nm}) \longrightarrow NO + O(^3P) \tag{R3}$$

the photolysis frequency $j(NO_2)$ is calculated by:

$$j(NO_2) = \int F_\lambda \times \sigma_{NO_2} \times \phi_{O(^3P)}\, d\lambda \tag{3}$$

Accordingly, the most versatile method to determine photolysis frequencies is spectroradiometry: the spectral actinic photon flux density F_λ is measured in the relevant UV/VIS spectral range and any photolysis frequency can be calculated, provided the corresponding molecular parameters σ and ϕ are known (Hofzumahaus et al., 1999). Other methods like chemical actinometry and filter radiometry have the disadvantage that they are process specific, but they can be advantageous for other reasons, e.g. for their absolute accuracy and easyness of maintenance for long-term operation, respectively (Kraus et al., 2000; Shetter et al., 2003; Hofzumahaus et al., 2004; Hofzumahaus, 2006).

The major technical difficulties related with the radiometric determination of F_λ in the atmosphere are (i) the quality of optical receivers for actinic radiation (with an ideally 4π-sr and angle-independent reception characteristics) and (ii) the accuracy

of measurements in the UV-B range that can be affected by stray-light. Both aspects are particularly challenging for aircraft measurements:

(i) In contrast to ground-based measurements where upward radiation in the UV range can often be neglected, aircraft deployments require separate measurements in the upper and the lower hemisphere. Because the optical receivers for actinic radiation have a vertical extension and limited horizontal shielding, cross-talks to the opposite hemispheres are unavoidable. These cross-talks and imperfections of the receivers in general require specific corrections. We attend to this difficulty in an accompanying paper where wavelength dependent correction factors are derived as a function of time, altitude and atmospheric conditions (Lohse and Bohn, 2017).

(ii) UV-B radiation in the troposphere and the lower stratosphere is strongly diminished by stratospheric ozone. Nevertheless, the remainder is extremely important for atmospheric chemistry because it can photolyze tropospheric ozone and form $O(^1D)$ (R1). To quantify the corresponding photolysis frequency $j(O^1D)$, accurate measurements of spectral actinic flux densities in the UV-B range are required (Eq. 2). Double-monochromator based spectroradiometers have excellent stray light suppression and high sensitivity for measurements of $j(O^1D)$ (Hofzumahaus et al., 1999; Shetter and Müller, 1999). However, the instruments have low time resolutions because the two monochromators have to be scanned synchronously to obtain a spectrum. This is a major drawback for high speed aircraft measurements where conditions can change rapidly through the influence of clouds, changing ground albedo or maneuvers in flight. A time resolution on the order of a second is therefore desired. Such a time resolution is achieved by single-monochromator based CCD detector array spectroradiometers (CCD-SR) (Eckstein et al., 2003; Jäkel et al., 2007; Petropavlovskikh et al., 2007; Stark et al., 2007). These instruments have the further advantage of a small size and weight, and of higher mechanical stability because they usually contain no motorized parts. On the other hand, measurements in the UV-B range suffer from an increased level of stray light that is typical for single-monochromator applications (Hofzumahaus, 2006). Therefore, a thorough treatment of stray light induced effects is a prerequisite for high quality measurements in the UV-B range with high time resolution.

In this work we describe the properties, the calibration and the data analysis of our CCD-SR based instruments for airborne measurements of spectral actinic flux densities and photolysis frequencies. The equipment was already employed on the research aircraft HALO (High Altitude and Long Range Research Aircraft) and on the Zeppelin NT during several missions. The applied type of CCD-SR is widely used for the determination of atmospheric photolysis frequencies. The instruments can be purchased ready for use and can directly provide photolysis frequencies. However, applications like airborne measurements require a more complicated post-flight data analysis. Moreover, quality assurance in any case requires regular re-calibrations based on as possible simple guidelines. We will therefore explain in detail how our instruments were calibrated and introduce a straightforward, reliable method how to deal with stray light influence in both laboratory calibrations and in the analysis of field data. To evaluate the approach, ground based comparisons with a double-monochromator reference instrument will be shown, as well as example data from a flight on HALO.

Figure 1. Basic components of a CCD array spectroradiometer system for airborne measurements. Receiver optics with optical fiber (black, front), spectrometer including monochromator and CCD array detector (middle), and cooling electronics (right).

2 Instrument properties

2.1 Spectroradiometers and data acquisition

The CCD spectroradiometers and optical receivers used in this work were developed by Meteorologie Consult GmbH (Metcon) specifically for measurements of spectral actinic flux densities and photolysis frequencies in the atmosphere. Five different
5 instruments that are identified by five-digit serial numbers were characterized and calibrated in the laboratory and pairwise used during several deployments on a Zeppelin-NT and on HALO between 2007 and 2015, as well as separately for occasional ground-based measurements. All instruments are similar in construction but exhibit somewhat variable individual properties. A slightly modified spectroradiometer of the same type was described previously by Jäkel et al. (2007).

The spectroradiometers are composed of combinations of a monochromator (Zeiss, MCS) and a back-thinned CCD detector
10 array (Hamamatsu, S7031-0906S, windowless), as well as operating electronics (tec5 AG) that are built into air-tight aluminium housings (approx. 30 cm ×15 cm×10 cm). These housings are connected with separate CCD Peltier cooling electronics (tec5 AG) and power supplies. Radiation is passed into the monochromators by 600 μm optical fiber feed-throughs terminated with SMA adapters. An actinic receiver optic can be attached tightly to the instrument housings or more flexibly via optical fibers with user-defined lengths. The latter option was chosen in this work because it is more convenient for aircraft installations.
15 Optical fiber lengths ranged between 2 m and 12 m. Dependent on the application, one or two spectroradiometers including electronics and a compact computer were built into 19 inch rack-mounts for operation in instrument flight racks. The basic components of a single instrument are shown in Fig. 1. More information on the optical receiver properties and related aircraft specific aspects are described in a separate paper (Lohse and Bohn, 2017).

Computer communication is established via USB or ethernet interfaces (tec5 AG). CCD data acquisition (16-bit signal counts, 0–65535) is controllable by a purpose-built software provided by Metcon. One of the features implemented in the software is the option to measure with different integration times quasi-simultaneously. Typically 4–5 integration times between 3 ms and 300 ms were used in field measurements and up to 1000 ms during laboratory calibrations. Longer integration times

5   are advantageous at low radiation levels to increase the signal-to-noise ratios (Sec. 2.2.2). On the other hand, shorter integration times may be necessary in parts of the spectra to avoid saturation of the CCD detectors. The idea is to piece together spectra with different integration times to an optimized spectrum with as long as possible integration times in different wavelength ranges. This optimization as well as the calculation of final actinic flux density spectra and photolysis frequencies is operable already during the measurements by the Metcon software. However, although this prompt analysis is useful for many applications, a

10   post-flight data analysis is required for airborne measurements by taking into account aircraft locations, rotation angles of the aircraft, and ambient conditions as explained in more detail in Sect. 3.1.

2.2   Laboratory characterisation and instrument calibration

2.2.1   Spectral range, resolution and wavelength accuracy

The employed monochromator type has a ceramic housing with a very low temperature drift (<0.01 nm/K). The thermostated

15   CCD detector is directly fixed to this housing making the setup mechanically insensitive to external temperature drifts. The holographic grating is blazed for 250 nm for optimum UV detection. Radiation enters the monochromator through a cross section converter and is dispersed onto the 532×64 pixel CCD array. By binning-operation the two-dimensional array is effectively used as a linear sensor array. The wavelength range covered by the spectroradiometers is roughly 260–660 nm with a mean spectral pixel distance of 0.8 nm. The relationship between the CCD pixel number (0–531) and the wavelength is

20   determined by manufacturer-based, instrument-specific third-order polynomial functions.

In order to verify the wavelength positions, spectra of a low pressure mercury pencil-lamp (Oriel) were recorded. After averaging over 50 single measurements, subtracting separately measured dark spectra (Sec. 2.2.2) and application of spectral sensitivities (Sec. 2.2.3), selected Hg emission lines in a range 290–550 nm were fitted with an empirical function $A(\lambda)$ to obtain instrument response functions and wavelength offsets:

25   $$A(\lambda) = a_0 \, \exp(-a_2(\lambda - a_1)^{a_3}) + B(\lambda) \tag{4}$$

Examples of emission line fits are shown in Fig. 2. The linear function $B(\lambda)$ allows to adjust for a tilted lamp background (lamp-specific continuous emission) and the parameter a_0 defines the fitted maximum of the line. The parameters a_2 and a_3 can be adjusted to match variable line shapes while the parameter a_1 denotes the central wavelength of a line with regard to the manufacturer-based wavelengths. The differences between a_1 and in-air line positions from the literature (Sansonetti et al.,

30   1996) are defined as wavelength offsets. Moreover, from the parameters a_2 and a_3 the full width at half maximum (FWHM) can be determined. Table 1 shows a summary of wavelength offsets and FWHM obtained with the five instruments, that typically do not exceed 0.2 nm and 2 nm, respectively.
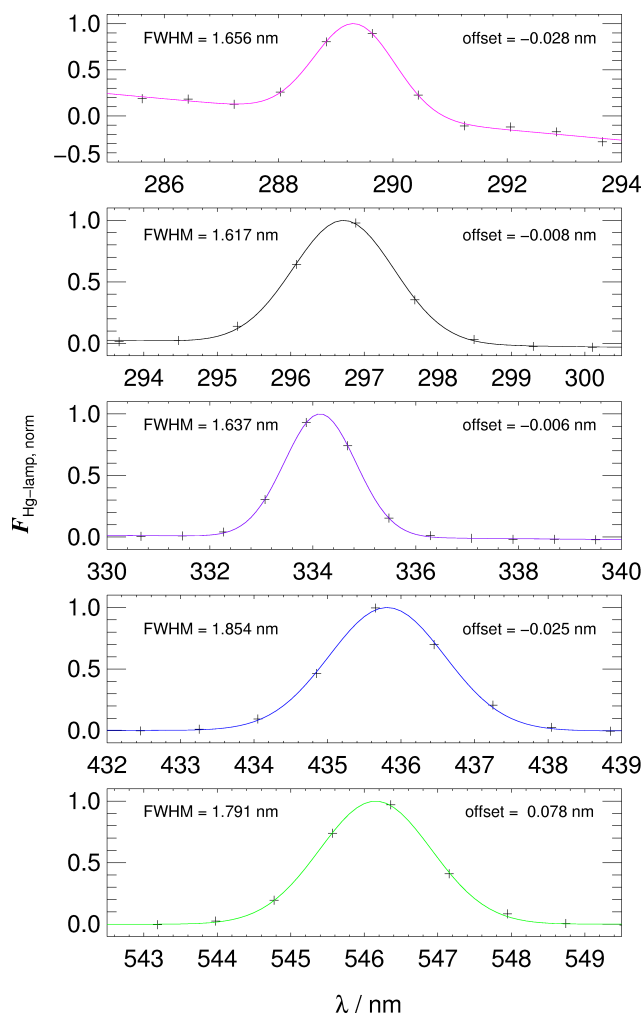
Figure 2. Selected sections of background corrected, normalized low-pressure Hg-lamp spectra obtained with instrument 62001 and corresponding emission line fits of Eq. 4 (full lines). Wavelengths correspond to manufacturer based third order polynomials of pixel numbers. Indicated wavelength offsets and FWHMs of emission lines were obtained from parameters a_1 to a_3 of Eq. 4.

Table 1. Wavelength offsets and slit function half-widths (FWHM) of spectroradiometers obtained by fitting Eq. 4 to Hg emission lines of a low pressure mercury lamp. Dependent on instrument, uncertainties correspond to standard deviations from 3–13 measurements during 3–9 year periods. Examples of emission line fits are shown in Fig. 2.

emission-line / nm	instrument				
	45853	62000	62001	62008	85235
	offset / nm				
289.360	−0.241±0.041	0.154±0.019	0.009±0.028	0.032±0.016	0.008±0.025
296.728	−0.172±0.010	0.170±0.009	0.018±0.021	0.051±0.016	0.014±0.024
334.148	−0.042±0.026	0.258±0.010	0.021±0.023	0.096±0.022	0.027±0.023
435.834	0.051±0.006	0.475±0.007	0.004±0.024	0.042±0.024	0.053±0.022
546.075	0.071±0.005	0.361±0.010	0.105±0.021	0.086±0.025	0.168±0.022
	FWHM / nm				
289.360	2.03±0.23	1.82±0.10	1.68±0.05	1.57±0.06	1.64±0.03
296.728	1.86±0.04	1.93±0.06	1.62±0.02	1.58±0.01	1.59±0.01
334.148	1.54±0.03	2.31±0.08	1.65±0.02	1.68±0.02	1.62±0.02
435.834	1.68±0.04	2.84±0.10	1.86±0.03	1.98±0.03	1.67±0.01
546.075	1.71±0.04	2.41±0.08	1.80±0.01	1.76±0.01	1.82±0.01

The quality of the results is limited by the relatively small number of data points that represent an emission line. Moreover, the assumption of symmetrical response functions and a linearly changing background may not strictly apply. Nevertheless, the reproducibility of the results is high, indicating that both parameters can be determined within ±0.05 nm. Wavelength shifts induced by reduced cabin pressures ($\geq$750 mbar) during airborne measurements are considered insignificant ($\leq$0.02 nm at 300 nm).

2.2.2 Dark signals, noise and signal-to-noise ratios

When optical receivers are covered and no radiation enters the spectroradiometers, dark signals can be recorded. As was already described by Jäkel et al. (2007), the dark signal for each pixel is composed of an electronic offset and a thermally induced dark current that increases with temperature and integration time. While the electronic offsets are fairly constant, dark currents are slightly different for each pixel but, except for noise, reproducible under temperature-controlled conditions. By averaging over, e.g. 100 single measurements, noise can be reduced and mean dark spectra for each integration time are obtained. Subtracting these dark spectra effectively removes the dark current-induced spectral structure that is underlying all measured spectra. This is particularly important under low-signal conditions. Examples of dark spectra for different integration times are shown in Fig. 3.
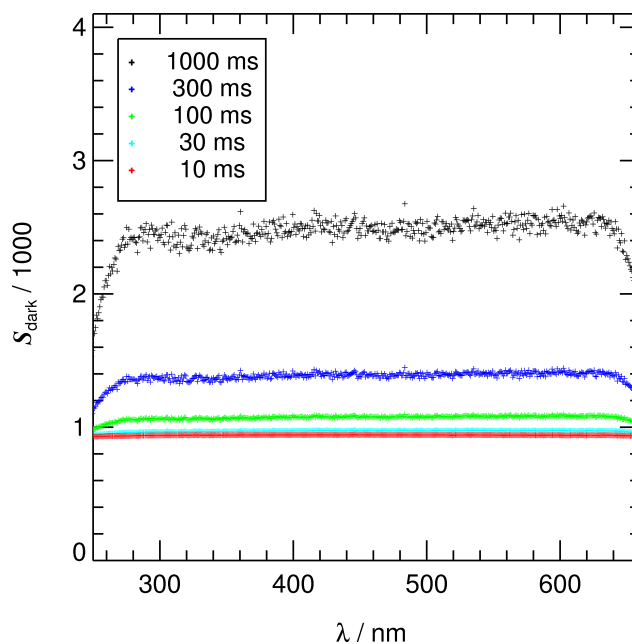
Figure 3. Mean dark signal spectra of instrument 62001 at different integration times. Dark signals S_{dark} are composed of an electronic background (≈ 900 for this instrument) and a dark current that increases with the square root of the integration time. Pixel-to-pixel variations represent reproducible structures. The corresponding mean noise of the dark signals is comparatively small and listed in Tab. 2

Because a slow, permanent change of dark signals with time cannot be excluded, it is useful to update dark spectra regularly. In addition dark signals may be subject to fluctuations that can be caused by external temperature changes or instabilities of the temperature control. The difference between a single measurement of the dark signal and the averaged dark signal may therefore deviate from zero more strongly than expected from the noise of the measurements. For atmospheric measurements this poses no problem because the remaining positive or negative background is determined together with a stray light induced background for each spectrum separately. This will be explained in more detail in Sect. 3.1. The main purpose to subtract mean dark spectra therefore is to obtain an approximate dark correction and to widely remove the dark current induced spectral structures visible in Fig. 3. This feature is also implemented in the Metcon software.

The noise of the dark signals was determined for each pixel by deriving standard deviations of repeated dark measurements. Table 2 lists the mean dark noise as a function of integration time for the employed instruments. The given ranges correspond to the variations of the noise in the wavelength range 280–650 nm. These ranges are small which means that all CCD pixels exhibit similar noise levels. The increase of dark noise with integration time on average follows a square root dependence as expected for thermally induced shot noise. The remaining noise towards zero integration time is considered a combination of instrument specific read-out noise and other off-chip noise.

The increase of instrument noise upon exposure to radiation was investigated by measurements with a 1000 W halogen lamp, operated with a highly stabilized power supply in the laboratory. The lamp was providing constant irradiation conditions that

Table 2. Mean noise of spectroradiometer dark signals as a function of integration time and corresponding standard deviations of mean noise in a wavelength range 280–650 nm. Examples of dark spectra are shown in Fig. 3.

integration-time / ms	instrument				
	45853	62000	62001	62008	85235
10	7.2±0.9	6.0±0.6	7.1±0.7	3.5±0.4	2.0±0.2
100	7.3±1.0	6.5±0.7	7.2±0.7	4.3±0.5	2.3±0.3
1000	8.3±1.1	10.4±1.1	11.4±1.3	8.7±2.6	4.4±1.6
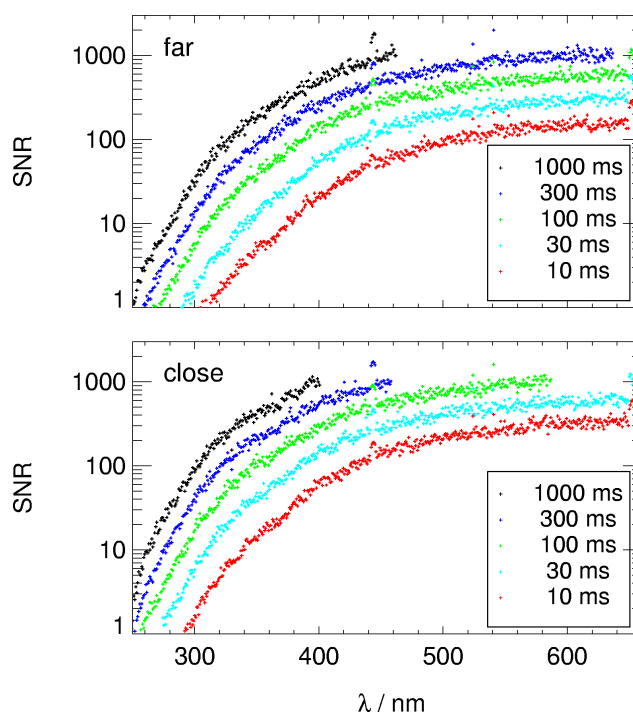
Figure 4. Signal-to-noise ratios (SNR) as a function of wavelength for different integration times from 1000 W irradiance standard measurements of instrument 62001. Upper panel: lamp distance 700 mm, lower panel: lamp distance 350 mm.

also served for spectral calibrations as described in the next section. The lamp was located at two distances from the optical receivers: at the certified distance for absolute calibrations of 700 mm and a smaller distance of about 350 mm. The smaller distance was mainly used to increase signals in the UV-B range. Noise was again derived from standard deviations of repeated measurements under the various signal levels produced by the lamp. Noise levels were found to increase with the square root of signals and integration times, respectively, consistent with photon induced shot noise. This also indicates that the noise of the lamp output is insignificant which is in line with the certified ±10 ppm current stability of the power supply.

Figure 4 shows an example of signal-to-noise ratios (SNR) of one of the instruments as a function of wavelength and integration time resulting from the measurements at the two selected distances from the lamp. All other instruments showed a comparable behaviour with SNR reaching a maximum of around 1000 close to saturation levels. For a given integration time, the SNR drop strongly towards short wavelengths because of decreasing lamp output, but also because of a decreasing spectral

5 sensitivity (Sect. 2.2.3). On the other hand, for a given wavelength, the SNR increase with the square root of the integration time and also improve at the shorter lamp distance unless saturation is reached. These advantages are utilized to optimize the calibration procedure in the following section.

2.2.3 Laboratory calibration

To calibrate the spectroradiometers, a PTB traceable spectral irradiance standard (Gigahertz-Optik, BN-9101) and a suitable

10 power supply (Opteema, OL83A) were used, utilizing the fact that irradiance and actinic flux density are identical upon normal incidence. However, for a point source like a lamp the certified distance between the lamp and the receiver has to be strictly adhered to, in this case 700 mm. For flat irradiance receivers this is straightforward but actinic radiation receivers are composed of quartz domes with an outer vertical extension of about 35 mm with no obvious reference plane. We therefore adapted the concept of equivalent plane receivers (EPR) described in detail by Hofzumahaus et al. (1999). Basically each actinic receiver

15 was characterized by distance dependent measurements of the lamp signal to evaluate the position of the EPR plane that is typically located 15–25 mm below the quartz dome tip and shows little wavelength dependence.

For calibrations, lamp and receiver were mounted on an optical bench at the reference distance between the lamp and the quartz dome tip with the help of a 700 mm spacer. Using the scale of the optical bench the receiver was then moved towards the lamp by the receiver specific EPR plane distance. During calibration measurements the receiver was placed into a black

20 box where the lamp radiation entered through a blind. The blind could be blocked for dark measurements. Alternatively a filter holder with a cutoff filter could be placed in front of the blind. The applied cutoff filter was a WG320 long pass filter (Schott) with an edge wavelength of 320 nm that safely removes all radiation below 300 nm (<1%) for separate stray light measurements in that range. Occasionally, further cutoff filters were used, in particular a WG360 with a 360 nm edge wavelength.

A typical calibration was made by a sequence of four cycles of 50–100 single measurements each, comprising different

25 integration times of up to 1000 ms: (1) dark, (2) lamp, (3) filter, and (4) dark. The receiver was then moved by 300-400 mm towards the lamp and the procedure was repeated. These cycles are referred to as far- and close-measurements. While for the far-measurements the correct distance to the lamp is important, the distance of the close-measurements is secondary, as long as a substantial increase of signals by a factor 3-5 is achieved. On the other hand, it is crucial that accurate dark signals are determined and subtracted. The dark measurements before and after the lamp measurements were routinely made to allow for

30 a check that there was no significant drift in dark signals during the calibration measurements.

The method to improve the calibration accuracy by using two lamp distances was recommended by the manufacturer and was already applied for diode array based spectroradiometers (PDA-SR) (Kanaya et al., 2003; Edwards and Monks, 2003; Jäkel et al., 2005; Bohn et al., 2008) and CCD-SR (Jäkel et al., 2007). The procedures described in the following were elaborated to improve the determination of stray light signals and to utilize several integration times to obtain optimized spectral sensitivities.
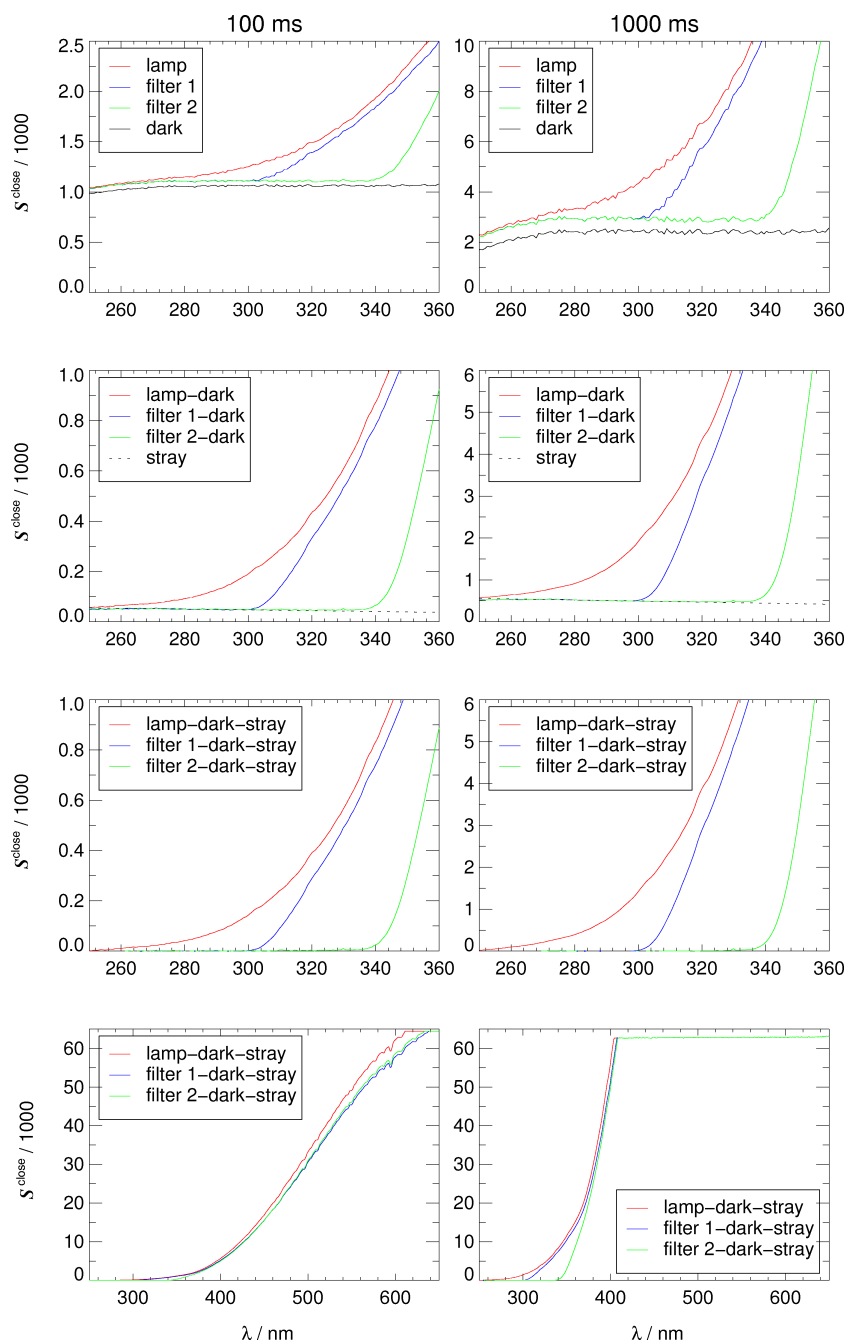
Figure 5. Example signals obtained during laboratory calibration measurements of instrument 62001 with two integration times and two cutoff filters. Upper panels: Total signals of lamp radiation with no filter (lamp), of lamp radiation with WG320 filter (filter 1), of lamp radiation with WG360 filter (filter 2), and dark signals (dark). In the second panels dark signals were subtracted and stray light signals were estimated by linear regressions in a range 265-300 nm (dashed lines) that are extrapolated over the whole spectral range. In the third panels also stray light signals were subtracted. In the last panels the full signal and wavelength range is shown. For 100 ms and 1000 ms integration times saturation was reached around 600 nm and 400 nm, respectively.

Spectral sensitivities D_λ were calculated using the following equation:

$$D_\lambda(\lambda, \Delta t) = \frac{S_{\text{lamp,corr}}^{\text{close}}(\lambda, \Delta t)}{E_\lambda^{\text{std}}(\lambda) \times f_1} \tag{5}$$

$S_{\text{lamp,corr}}^{\text{close}}(\lambda, \Delta t)$ are spectroradiometer signals from the close-measurements at different integration times Δt, corrected for dark and stray light signals. $E_\lambda^{\text{std}}(\lambda)$ are the certified spectral irradiances of the standard lamp in the required spectral photon flux density units ($\text{cm}^{-2}\text{s}^{-1}\text{nm}^{-1}$) and f_1 is the mean ratio of corrected signals from close- and far-measurements. These quantities will be explained in more detail in the following. Note that all S variables are dependent on integration time and wavelength which will not be indicated explicitly in the following equations for brevity.

Close-measurement signals were corrected by subtraction of dark (S_{dark}) and estimated stray light signals ($S_{\text{scat}}^{\text{close}}$) corrected by a further scaling factor f_2^{close}:

$$S_{\text{lamp,corr}}^{\text{close}} = S_{\text{lamp}}^{\text{close}} - S_{\text{dark}} - S_{\text{scat}}^{\text{close}} \times f_2^{\text{close}} \tag{6}$$

Figure 5 shows examples of signals from close-measurements for two integration times of 100 ms and 1000 ms. In the uppermost panel, dark signals, lamp signals without filter ($S_{\text{lamp}}^{\text{close}}$), and lamp signals with two different cutoff filters (WG320, WG360) ($S_{\text{filter}}^{\text{close}}$) are plotted. For better visibility the wavelength range was confined to 250–360 nm. In the second panel, dark signals were subtracted which also removes the dark current induced fluctuations, as intended (Sect. 2.2.2). The remaining signals come from the desired lamp radiation and underlying stray light. Obviously the $S_{\text{scat}}^{\text{close}}$ can only be determined from measurements with cutoff filter in a wavelength range where the filter safely blocks radiation, i.e. below 300 nm in the case of a WG320 filter:

$$S_{\text{scat}}^{\text{close}} = S_{\text{filter}}^{\text{close}} - S_{\text{dark}} \quad (< 300 \text{ nm}) \tag{7}$$

For all instruments $S_{\text{scat}}^{\text{close}}$ could be linearly fitted in good approximation in a range around 265–300 nm. The $S_{\text{scat}}^{\text{close}}$ at greater wavelengths are then approximated by linear extrapolations over the full spectral range, as indicated by the dashed lines in the upper middle panels of Fig. 5. The validity of this extrapolated stray light signal is confirmed in this example by the additional measurements with the WG360 filter showing an almost identical stray light background compared to the extrapolation. Since the importance of stray light quickly diminishes with increasing wavelength and lamp signals, the adapted procedure is preferred here because it is most accurate in a range <350 nm where the determination of D_λ is affected by stray light. A modification of this procedure was only necessary for the oldest instrument 45853 where a stronger wavelength dependence and a leveling-off of the stray light induced signal around 340 nm was observed. For 45853 the stray light level was generally increased compared to the other instruments.

The factor f_2^{close} in Eq. 6 accounts for the fact that the filter slightly diminishes radiation also well above its cutoff wavelength by normal reflections at the filter surfaces. Accordingly, also stray light is slightly smaller during the filter measurements. Because a large fraction of stray light ($\approx 50\%$) originates in the unmeasured VIS and NIR range of the spectrum, as was verified by cutoff filters with longer edge wavelengths, f_2^{close} was determined in a range 640 ± 10 nm.

$$f_2^{\text{close}} = \frac{S_{\text{lamp}}^{\text{close}} - S_{\text{dark}}}{S_{\text{filter}}^{\text{close}} - S_{\text{dark}}} \quad (640 \pm 10 \text{ nm}) \tag{8}$$
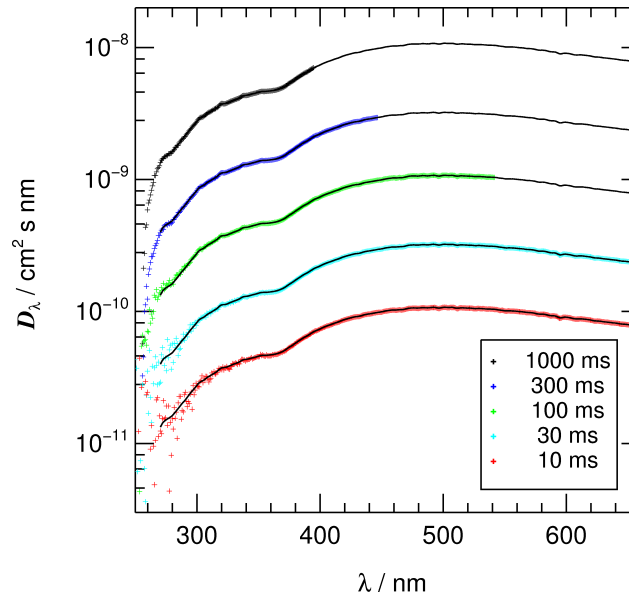
Figure 6. Spectral sensitivities of instrument 62001 at different integration times. Full lines show an optimized sensitivity that was scaled dependent on integration time according to Eq. 10. Data points show the separately measured sensitivities for comparison.

The f_2^{close} typically ranged around 1.05 and were found to be independent of integration time, as expected. Consequently, mean values of f_2^{close} were applied using integration times not affected by saturation. For the spectral sensitivities the factor f_2^{close} is negligible above 310 nm ($<$1%) but it becomes increasingly important at shorter wavelengths ($\approx$10% at 280 nm). An exception is again instrument 45853 with a greater influence of f_2^{close} because of an increased stray light level.

5   In the lower middle panels of the Fig. 5 the scaled stray light signals were subtracted returning the $S_{\mathrm{lamp,corr}}^{\mathrm{close}}$ according to Eq. 6 (red curves). In the lowermost panels the same data are shown over the full signal and wavelength ranges. For the longest integration time of 1000 ms saturation is evident above 400 nm while for 100 ms saturation sets in around 600 nm.

Finally the factor f_1 in Eq. 5 was determined from mean ratios of corrected close- and far- signals:

$$f_1 = \frac{\overline{S_{\mathrm{lamp,corr}}^{\mathrm{close}}}}{S_{\mathrm{lamp,corr}}^{\mathrm{far}}} \qquad (9)$$

10   As long as the denominator and the numerator in Eq. 9 were below saturation and above a certain, noise insensitive threshold ($\approx$200), respectively, also these factors were found to be independent of wavelength and integration times. The scaling factor f_1 is important because it establishes the final connection between the SNR-improved close-measurements and the far-measurements at the correct lamp distance.

Although it makes a very minor difference, in the calculation of D_λ according to Eq. 5, the lamp spectrum E_λ was shifted
15   by interpolated offset wavelengths of the spectroradiometers, i.e. when wavelengths are corrected by their offsets, the D_λ correspond to the correct wavelengths.

The procedure described so far yields spectral sensitivities for each integration time that was used during the calibrations. These sensitivities expectedly scale with the integration times:

$$D_\lambda(\lambda, \Delta t_2) = D_\lambda(\lambda, \Delta t_1) \times \frac{\Delta t_2}{\Delta t_1} \tag{10}$$

This relation was used to derive consistent, optimum sensitivities for all integration times, by favoring measurements with the

5   longest possible Δt_1 as long as no saturation was reached. Practically, a master sensitivity file was produced for the maximum integration time of 1000 ms. The data were then scaled to obtain sensitivities for other integration times. An example of the resulting sensitivities is shown in Fig. 6 (full lines) together with the measured values. With decreasing integration time and wavelengths, measured data expectedly start to scatter around the optimized sensitivities. The common decrease of sensitivities towards shorter wavelengths is, by the way, not caused by a decrease of CCD sensitivity but mainly by the actinic radiation

10   receiver through which only a small fraction of multiply scattered radiation is eventually transmitted.

It should be noted that the Metcon software uses an inverse definition of sensitivity compared to Eq. 5, as well as spectral energy flux density units (W m^{-2} nm^{-1}) rather than spectral photon flux densities (cm^{-2} s^{-1} nm^{-1}). Accordingly, the tabulated sensitivities decrease with integration times and have different dimensions. The conversion is straightforward but should be kept in mind for comparisons and in any user-developed evaluation software.

15   The absolute sensitivities obtained for all instruments are comparable and roughly correspond to that shown by Jäkel et al. (2007) for their original setup. However, for the majority of their measurements Jäkel et al. (2007) employed a UV transmitting filter (UG5, Schott) that strongly diminished the sensitivity above 400 nm. Through this modification they reduced stray light, avoided saturation of the CCD in the VIS range and could therefore work with a single integration time of 200 ms during field measurements. However, the stray light reduction by a UG5 is only about 50% because this filter still transmits a substantial

20   fraction of NIR radiation. At the same time the UG5 transmittance is only 1% around 600 nm which could introduce a stray light issue in a spectral range important for NO_3 photolysis. In contrast to the UV-B range where the atmospheric cut-off provides a means to routinely determine the variable stray light contribution during field measurements (Sec. 3.1), there is no such possibility in the VIS range. We therefore accept the inconvenience of multiple integration times and of increased stray light to exclude any interference outside the UV-B. Nevertheless, the approach by Jäkel et al. (2007) is generally supported for

25   atmospheric measurements, unless small values of $j(NO_3)$ are of interest. Jäkel et al. (2007) also compared the performance of PDA-SR and CCD-SR in the UV range and clearly demonstrated the advantage of CCD-SR because of the higher sensitivity. Also Eckstein et al. (2003) described a CCD-SR with similar sensitivities and a time resolution of 3 s. A direct comparison of spectral sensitivities is difficult because a teflon sphere was used for 4π measurements of spectral actinic flux densities with a single receiver.

30   **2.2.4   In-field calibrations**

For technical reasons, in-field calibrations with a 1000 W standard (as described in the previous section) are difficult, especially for the final setup on an aircraft. On the other hand, calibrations are necessary to monitor any sensitivity change caused by transportation or the installation process which usually requires that optical fibers are disconnected, rearranged and recon-
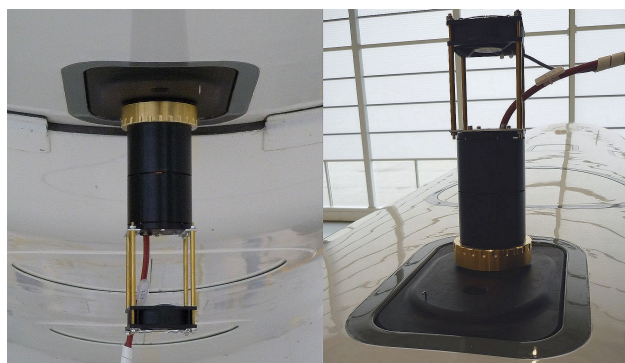
Figure 7. In-field calibration setup with traveling standard lamps attached to receiver optics on HALO. Left: bottom fuselage, right: top fuselage.

nected. Therefore, secondary calibrations with small 45 W lamps acting as traveling standards were made. These lamps have specially designed housings that can be fixed directly at the optical receivers without any interference to receiver mountings or optical fibers. Moreover, the lamps are ventilated and shielded against ambient radiation so that calibrations are feasible during daylight. Figure 7 shows the setup during a calibration in the HALO hangar. Spectra of two 45 W lamps were routinely

5   recorded directly after the laboratory calibration with the irradiance standard, as well as in the aircraft hangars before and after the instrument deployments. The use of two lamps allows for consistency checks and assures that the transfer calibration is not lost in case of a lamp failure.

Figure 8 shows examples of measurements that were made with instrument 62001 before and after a deployment on HALO. Ratios of dark signal corrected lamp signals are shown representing the relative change of spectral sensitivities compared to the

10   laboratory calibration. As in the laboratory, 100 single dark and lamp measurements were always averaged. The large scatter of the ratios at short integration times and below 350 nm results from the low output of the 45 W lamps that is comparable to far-measurements with a 1000 W lamp. Moreover, for technical reasons the optional use of cutoff filters is not feasible for the small lamps. As a result, the change of spectral sensitivities in the UV-B cannot be determined accurately. On the other hand, little, if any spectral variations have been observed above 350 nm. Therefore, extrapolations of second-order polynomials

15   were used below 350 nm that were fitted in a range 350–650 nm. The full lines in Fig. 8 indicate the corresponding ratios that consider the measurements with both lamps and that were finally applied to scale the laboratory based spectral sensitivities. Typically the scaling factors ranged between 0.95 and 1.05 which means that laboratory calibrations were widely reproducible after transportation and aircraft installation. Moreover, measurements before and after deployments were typically within 2%, i.e. calibrations were stable as long as the setups remained unchanged. Finally, the results obtained with two different lamps

20   were usually similar within 1%, giving additional confidence in the field-calibration procedure.
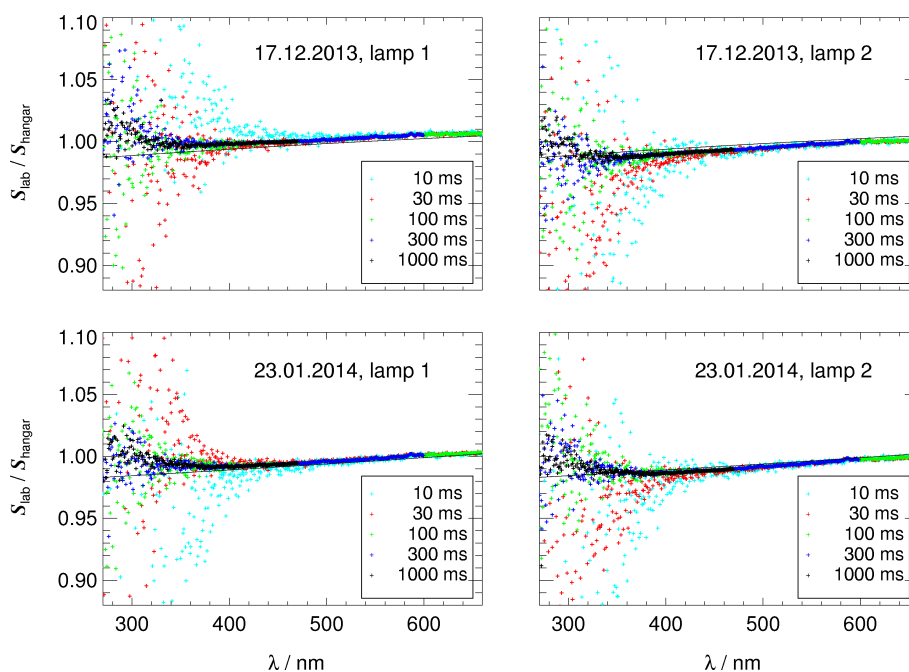
Figure 8. Ratios of dark-corrected signals of 45 W traveling standard lamps obtained with instrument 62001 after a laboratory calibration on 03.09.2013 (S_{lab}) and directly before and after a deployment on HALO (S_{hangar}). Two lamps were used each during laboratory and hangar measurements (left and right panels). Data points show individual measurements for different integration times, full lines the finally applied scaling factors for each date (polynomial fits, mean of measurements with both lamps on a specific date).

2.2.5 Calibration accuracy

The overall accuracy of the spectral calibrations is determined by a number of factors. Firstly by the certified accuracy of the irradiance standard which is 3–4%, dependent on wavelength. The accuracy of the lamp current produced by the power supply is certified with 0.01% which translates to a maximum 0.1% uncertainty of the irradiance output (manufacturer information). A further 1.5% uncertainty is calculated from an estimated 5 mm uncertainty of the position of the EPR reference plane. Because consistent results were obtained for different wavelengths and integration times, the accuracy of the factor f_1 is within 0.5%.

The uncertainties related with the subtracted stray light signals are more difficult to assess. In the most sensitive range below 300 nm the applied linear approximation is leading to deviations less than 1% from the measured values. The uncertainty of the extrapolation beyond 300 nm is increasing with wavelength but the importance of stray light also quickly diminishes with increasing wavelength. Moreover, an additional 1% uncertainty is estimated for the scaling factor f_2 of the stray light signal. Assuming a total 3% uncertainty of the subtracted stray light signals, changes in sensitivities between 1% at 300 nm and 0.02% around 400 nm are obtained (4% and 0.1% for instrument 45853).

Finally, the accuracy of in-field calibrations is estimated 2% in the UV-B and 1% for the UV-A and VIS range. Taking all these factors together results in total uncertainties between 5–6% at 300 nm and 4% at 650 nm.

2.2.6 Detection limits and cutoff wavelengths

During laboratory calibrations measurements were repeated to reduce the noise. For example, averaging over 100 single measurements reduces the noise by a factor of $\sqrt{100}$. Instrument noise therefore plays no important role for the determination of spectral sensitivities. Also during field measurements, averaging is possible and often applied. However, averaging also leads

5 to a reduction of time resolution which may not be useful for airborne measurements. Therefore, at maximum time resolution the noise of single measurements determines the detection limits. In order to estimate these limits, a noise-equivalent spectral actinic flux density (F_λ^{NE}) can be defined by the ratios of the dark noise obtained in Sect. 2.2.2 ($S_{\mathrm{dark}}^{\mathrm{NE}}$) and spectral sensitivities:

$$F_\lambda^{\mathrm{NE}}(\lambda, \Delta t) = S_{\mathrm{dark}}^{\mathrm{NE}}(\lambda, \Delta t)/D_\lambda(\lambda, \Delta t) \tag{11}$$

10 The corresponding spectra for instrument 62001 are shown in Fig. 9 as an example. Expectedly, the F_λ^{NE} increase with decreasing wavelength and are lower for longer integration times. Absolute values are comparable with results obtained by Jäkel et al. (2007) in the UV range but smaller in the VIS range because no UG5 filter was used in this work. Detection limits are usually defined as the three-fold of the noise-equivalent values which can be further improved by a factor $\sqrt{N}$ upon averaging over N single measurements. However, these detection limits should be considered a theoretical minimum because additional

15 uncertainties from stray light and varying background under field conditions are not included.

Corresponding noise estimates in terms of photolysis frequencies were derived by multiplying the noise-equivalent spectra with random noise for each pixel followed by calculations of photolysis frequencies according to Eqs. 2 and 3 as an example. The resulting standard deviations for $j(\mathrm{O}^1\mathrm{D})$ and $j(\mathrm{NO}_2)$ for instrument 62001 are listed in Tab. 2 for different integration times. In these calculations the wavelength range was confined to the atmospherically relevant range above 280 nm. For the

20 longest integration time of 1000 ms the noise limits correspond to 0.1% and 0.0001% of typical maximum values of $j(\mathrm{O}^1\mathrm{D})$ and $j(\mathrm{NO}_2)$, respectively. For the shortest integration time of 10 ms these numbers increase by factors of 40–50, still sufficiently low for $j(\mathrm{NO}_2)$, but not for $j(\mathrm{O}^1\mathrm{D})$. Also for the photolysis frequencies a factor of three should be applied to estimate detection limits which are again considered theoretical minima unless averaging is permitted.

In any case, the detection limits of $j(\mathrm{O}^1\mathrm{D})$ can be significantly reduced by further confining the wavelength range, for

25 example to wavelengths above 300 nm (Tab. 2). The reason for this reduction is that $\mathrm{O}(^1\mathrm{D})$ formation mainly takes place in a range below 320 nm where the corresponding product $\sigma \times \phi$ in Eq. 2 increases strongly towards shorter wavelengths. For $j(\mathrm{NO}_2)$ no such reduction of detection limits is obtained because the term $\sigma \times \phi$ is distributed over a wider wavelength range, covering the complete UV with a broad peak around 380 nm. Of course, whether or not such a confinement of the wavelength range is justified depends on measurement conditions because the wavelength below which atmospheric actinic flux densities

30 can be safely set to zero because it becomes negligible in terms of $j(\mathrm{O}^1\mathrm{D})$ is mainly determined by total ozone columns and solar zenith angles.

In the following we define so-called cutoff-wavelengths below which spectral actinic flux densities safely drop below values of $5 \times 10^9 \mathrm{cm}^{-2}\mathrm{s}^{-1}\mathrm{nm}^{-1}$ which roughly corresponds to the F_λ^{NE} around 300 nm for the longest integration times of the spectroradiometers (Fig. 9). Practically, the cutoff wavelengths were derived from model calculations of clear-sky downward
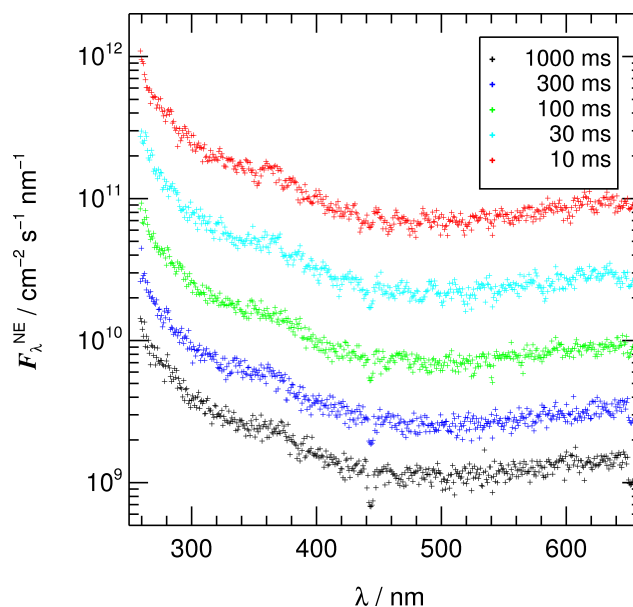
Figure 9. Noise-equivalent actinic flux density F_λ^{NE} of instrument 62001 for single measurements at different integration times according to Eq. 11.

Table 3. Standard deviations of photolysis frequencies obtained with random noise corresponding to noise-equivalent actinic flux densities (Eq. 11) for instrument 62001. The spectral range is 280–650 nm, for numbers in brackets 300–650 nm.

| integration- | noise equivalent photolysis frequency / s^{-1} | |
time / ms	$j(\mathrm{O}^1\mathrm{D})$	$j(\mathrm{NO}_2)$
10	2.6×10^{-6} (1.3×10^{-7})	5.9×10^{-7} (5.8×10^{-7})
30	8.4×10^{-7} (4.6×10^{-8})	2.0×10^{-7} (1.9×10^{-7})
100	2.6×10^{-7} (1.4×10^{-8})	6.1×10^{-8} (6.0×10^{-8})
300	9.9×10^{-8} (5.4×10^{-9})	2.4×10^{-8} (2.3×10^{-8})
1000	3.9×10^{-8} (2.2×10^{-9})	1.2×10^{-9} (9.4×10^{-9})

spectral actinic flux densities using the libRadtran radiative transfer model (Mayer and Kylling, 2005; Emde et al., 2016). Calculations were made for altitudes of 0 km (ground-based and Zeppelin measurements) and 15 km (aircraft measurements) covering ozone columns of 100–600 DU (Dobson units) and solar zenith angles (SZA) of 0–88°. For both altitudes lookup tables were produced ranging between 280 nm (15 km, SZA=0°, 100 DU) and 309 nm (0 km, SZA=88°, 600 DU). Typically

5   the differences between 0 km and 15 km cutoff wavelengths are no more than around 2 nm. The $j(\mathrm{O}^1\mathrm{D})$ fractions attributable to the wavelength ranges below the cutoffs are always insignificant (<0.1%).

The cutoff wavelengths were not only introduced here to reduce the noise of $j(\mathrm{O^1D})$ measurements but also to determine the variable wavelength limits below which atmospheric stray light signals can be determined in a similar way as during laboratory measurements with cutoff filters. This approach will be applied in the next Section.

3 Field measurements and data analysis

3.1 Field data evaluation

3.1.1 Auxiliary data

In order to simplify the data analysis of aircraft measurements, sets of all required additional parameters are collected in separate files after synchronisation with the spectroradiometer data. These parameters are static temperature and pressure; longitude, latitude and altitude; pitch, roll and yaw angles; solar zenith and azimuth angles; total ozone columns, and cutoff wavelengths. Except for the last four, these parameters were routinely provided by the aircraft operators. Solar zenith and azimuth angles were calculated based on date, time and aircraft locations. Ozone columns were interpolated temporally and spatially along the flight tracks from assimilated daily global fields of satellite-derived ozone columns (www.temis.nl, Eskes et al. (2003)). Finally, cutoff wavelengths were extracted from the respective lookup-tables (Sect. 2.2.6) using solar zenith angles and total ozone columns as input.

3.1.2 Spectral actinic flux densities

During atmospheric measurements several integration times between 3 ms and up to 300 ms were used and the raw data were saved with or without further averaging dependent on the desired time resolution of spectral actinic flux densities. No averaging resulted in a maximum time-resolution of 0.8–0.9 s while 10 s averages typically covered 12–13 single measurements for each integration time. 1 and 3 s averages were finally used for airborne measurements on HALO and the Zeppelin, respectively and 10–60 s averages for ground-based measurements.

Figure 10 shows an example of raw data from a HALO flight at an altitude of 13 km. As was mentioned in the introduction, airborne deployments always comprised simultaneous measurements with two CCD-SR taking separate 2π-sr measurements of downward and upward actinic flux densities in the upper and lower hemisphere, respectively. In Fig. 10 data from the lower hemisphere are shown on the left hand side, those from the upper hemisphere are on the right hand side.

The first step in the data analysis is the subtraction of mean dark signals to remove the dark-signal-induced structures from the spectra (Sect. 2.2.2). For better visibility this is shown in the uppermost panels for the UV-B range and the longest integration times of 300 ms. The second step is to apply a linear regression in a wavelength range between 270 nm and the variable cutoff wavelength to determine stray light signals plus any remaining positive or negative offset in dark signals. The dashed lines in Fig. 10 show the corresponding regression lines. The cutoff wavelength in this example was 291 nm. The linearly approximated stray light signals were then subtracted resulting in background and stray light corrected signals (blue lines).
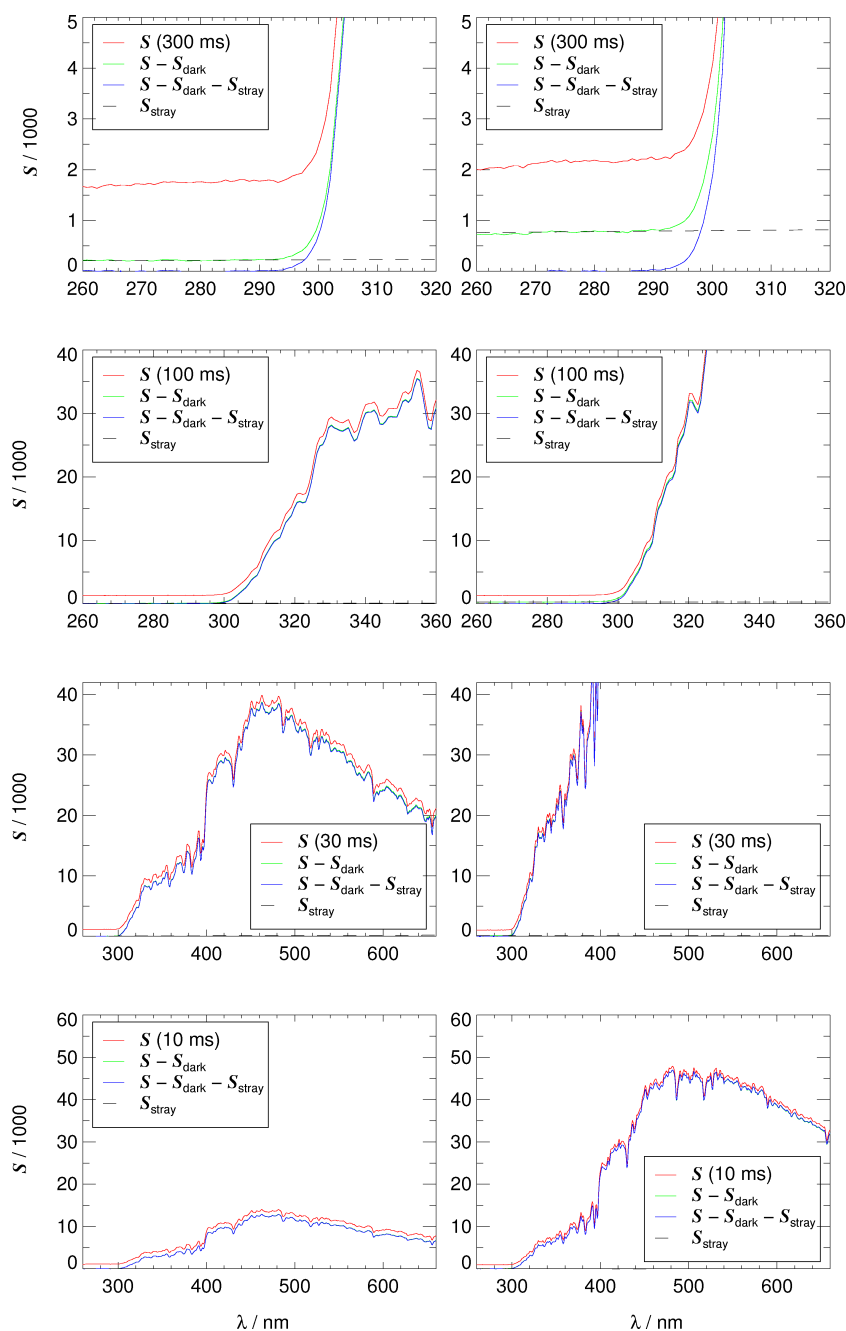
Figure 10. Examples of flight raw data and evaluations of instruments 62000 (lower hemisphere, left) and 62001 (upper hemisphere, right). Different colors indicate the evaluation steps: raw data (red), background subtraction (green) and stray light subtraction (blue). Stray light (dashed black lines) was determined by linear regression of background corrected signals in a range 270 nm to 291 nm (cutoff wavelength). Data were obtained during a HALO flight on 20 Dec 2013 17:30 UTC over the North Atlantic (15.0N, -55.9E, 13.2 km) under conditions with few scattered low-lying clouds at an SZA of 47° and an ozone column of 245 DU. The different panels show the corresponding data for different integration times and wavelength ranges.
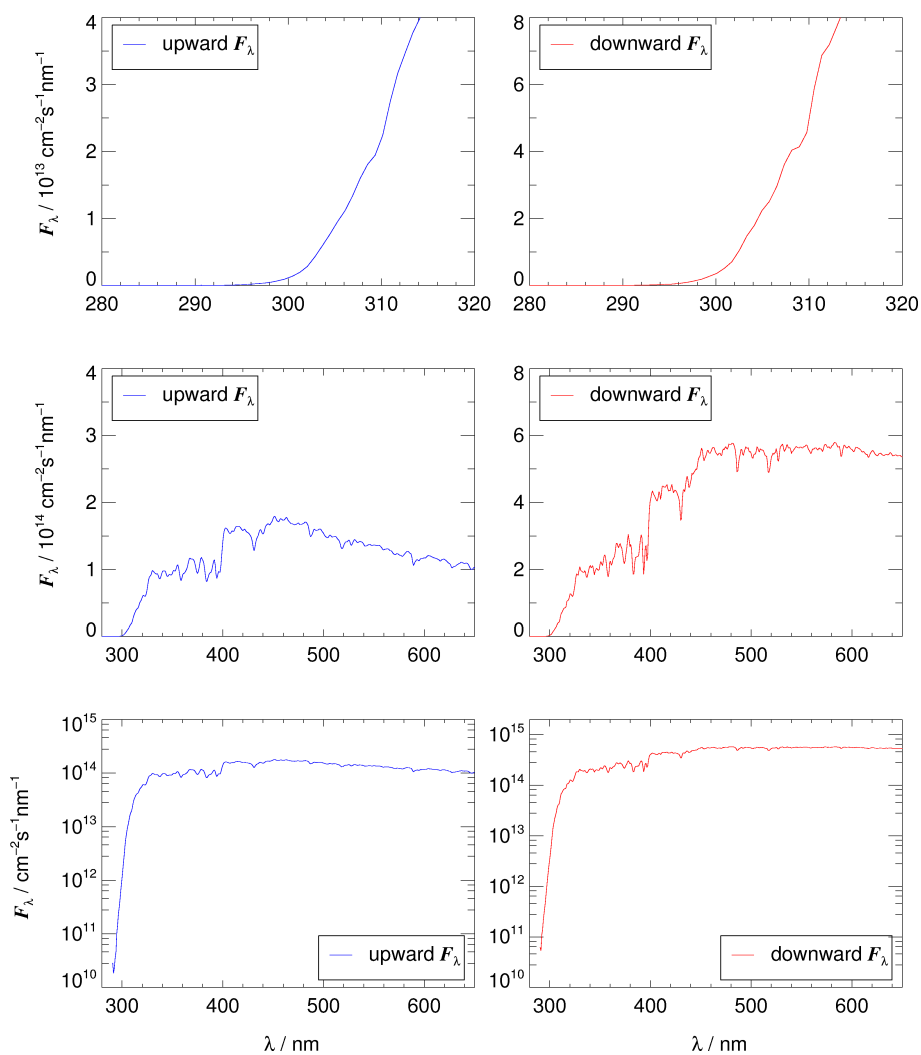
Figure 11. Evaluated upward (left) and downward (right) spectral actinic flux densities from the data shown in Fig. 10 in different representations. The sharp increase in the UV-B range in the upper panels is similar for upward and downward radiation, but absolute values differ by about a factor of three. The middle and lower two panels show the full wavelength and actinic flux density ranges in linear and semi-logarithmic representations, respectively.

The additional panels in Fig. 10 show the corresponding data for shorter integration times and extended wavelength ranges, also indicating the variable saturation limits. Evidently, also under atmospheric conditions the potential impact of stray light signals quickly diminishes with increasing wavelength, i.e. the uncertainty related with the linear extrapolation of stray light signals to wavelengths of up to around 650 nm is insignificant. Tests with various cutoff filters confirmed that there are no

5 significant stray light induced structures in the investigated spectral range. In a third step, spectral calibrations were applied to derive spectral actinic flux densities for each integration time. To account for wavelength offsets in these calculations signals were interpolated to offset-corrected wavelengths. Again this is making very little difference but is leading to correct F_λ if the wavelengths are offset-corrected. Finally, starting with the longest available integration time, any missing data caused by saturation were successively replaced by data obtained with shorter integration times until the spectrum was complete.

10 Moreover, data at wavelengths below the cutoff were set to zero (Sect. 2.2.6). The optimum spectra were then saved for each instrument. This procedure was applied for all measurements along the flight tracks. The final spectra of the examples in Fig. 10 are shown in Fig. 11 in different representations to illustrate the typical sharp increase in the UV-B range, the spectral range and differences in upward and downward actinic flux densities.

In a further step, corrections were made to compensate for imperfections of the optical receivers. These corrections differ for

15 HALO, Zeppelin and ground-based measurements and are usually ranging below 5% with respect to total actinic flux densities, except for airborne measurements close to sunrise or sunset. In addition data were sorted out where pitch and roll angles exceed certain limits or where shading of the receivers by aircraft structures may influence the measurements. More details on these optical receiver related corrections are given elsewhere (Lohse and Bohn, 2017).

Total actinic flux density spectra can be produced by adding up data from the upper and the lower hemisphere. However,

20 because the two measurements are independent of each other, this requires a thorough temporal and spectral synchronization, also considering the different instrument response functions. Generally, a separation of upward and downward actinic flux densities is desired, for example for comparison with model calculations. Total actinic flux density spectra were therefore not produced routinely.

3.1.3 Photolysis frequencies

25 Photolysis frequencies were calculated from actinic flux density spectra according to the examples given in Eqs. 2 and 3 by inserting respective molecular data of the photolysis processes under consideration. Measured spectra and molecular data from the literature were interpolated to a common wavelength grid with 0.1 nm resolution and added up after multiplication (Hofzumahaus et al., 1999; Bohn et al., 2008). The wavelength offsets were also considered in these calculations. Because wavelength offsets were corrected to within 0.05 nm of the true values, the remaining uncertainties are insignificant for the

30 accuracy of photolysis frequencies (Hofzumahaus et al., 1999). The spectral resolutions (FWHM) listed in Tab. 1 are expected to lead to a slight overestimation of $j(O^1D)$ ($\approx$2%) and an underestimation of $j(HCHO)$ ($\approx$3%) while no significant influence on $j(NO_2)$ is expected according to previous studies (Hofzumahaus et al., 1999; Bohn et al., 2008). $j(O^1D)$ and $j(HCHO)$ are more affected by limitations of spectral resolutions because of the sharp increase of atmospheric actinic flux densities in the UV-B range and narrow spectral features of the HCHO absorption spectrum, respectively.

In accordance with the actinic flux densities, contributions of photolysis frequencies were derived separately for the upper and the lower hemisphere. These contributions were then added up after time synchronization to obtain the photochemically relevant total photolysis frequencies. Examples of photolysis frequencies obtained during airborne measurements are shown in Sect. 3.3.

3.2 Evaluation by ground-based comparisons

In order to evaluate the accuracy of photolysis frequencies obtained in field measurements, ground-based comparisons of the CCD-SR with a double-monochromator based reference instrument (DM-SR) were routinely made. Typically before and after a deployment, the instruments were set up on a roof platform for parallel measurements of downward spectral actinic flux densities for a couple of days.

The reference instrument was described in detail elsewhere (Hofzumahaus et al., 1999; Bohn et al., 2008). As was mentioned in the introduction, the main advantage of the DM-SR is an effective stray light suppression. However, the scanning procedure leads to a limited time resolution and reduced accuracy under variable atmospheric conditions. To minimize this limitation, the DM-SR measurements were confined to a wavelength range 280–420 nm, the spectral range most important for the determination of photolysis frequencies. This resulted in a time-resolution of about 2 min. The instrument was operated at a FWHM of 1 nm, i.e. the spectral resolution was slightly better than that of the CCD-SR (Tab. 1).

Figure 12 shows examples of actinic flux density spectra obtained simultaneously with the DM-SR and instruments 62000 and 62001. The spectra were selected for stable, clear-sky conditions to avoid deviations caused by DM-SR scanning operations. The CCD-SR spectra are 10 s averages obtained with maximum 300 ms integration times for both instruments. The first and the second panel each show the expected sharp increase of actinic flux densities in the UV-B range that is reproduced similarly by all three instruments. In the third panel the comparison is extended to the complete spectral range covered by the DM-SR. Generally good agreement is obtained except for sharp spectral features that are resolved more accurately by the reference instrument because of a smaller FWHM. Minor optical receiver specific corrections ($<5\%$) were already included in this comparison (Lohse and Bohn, 2017).

The lowermost panels of Fig. 12 show the increase of UV-B spectral actinic flux densities in semi-logarithmic plots where more details can be recognized. Here also data below the cutoff wavelength (vertical lines) that are usually set to zero for the CCD-SR are shown for comparison. In this wavelength range data scatter around zero as expected, albeit with different residual noise. For the DM-SR the noise is unaffected by stray light and similar to nighttime values corresponding to F_λ^{NE} $\approx 1\times10^9$ cm^{-2} s^{-1} nm^{-1}. Thus the DM-SR noise is smaller by a factor of about 10 compared to the F_λ^{NE} of the CCD-SR in the 280–290 nm range for 300 ms integration time (Fig. 9). The residual noise for both CCD-SR is accordingly greater but, considering that 10 s averages are shown, it is in fact greater than expected. A closer look at the CCD-SR residual noise during day and night reveals that while in the dark the noise is consistent with the F_λ^{NE} obtained in the laboratory measurements (Fig 9), it is increased by a factor of up to 2–3 during daytime. This is attributed to additional noise induced by stray light.
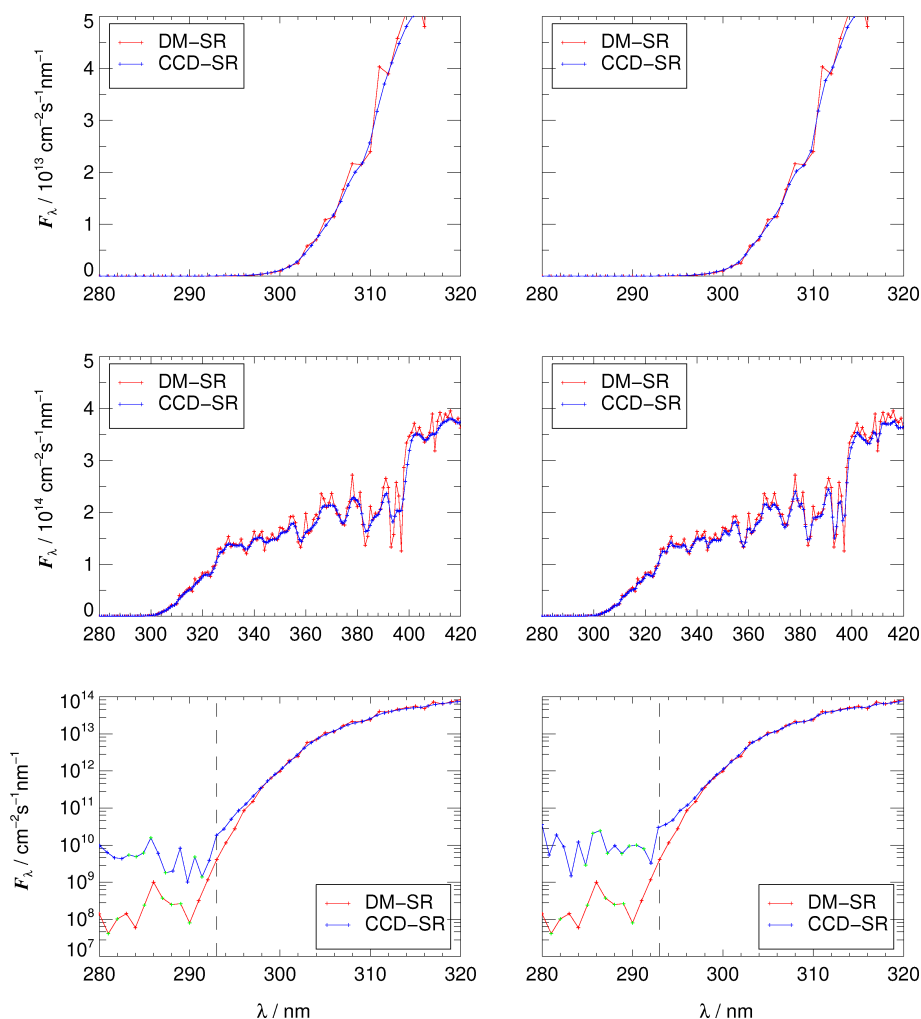
Figure 12. Comparisons of actinic flux density spectra obtained on the ground with a double-monochromator based reference instrument (DM–SR) and instruments 62000 (left) and 62001 (right). Measurements were made on 01 Aug 2013 at Jülich (Germany) under clear-sky conditions. The examples were taken around 12:00 UTC at a solar zenith angle of 32° and an ozone column of 340 DU. The different representations emphasize the increase of actinic flux densities in the UV-B range (upper panels) and the dynamic range of data (middle panels). Green data points in the semi-logarithmic plots (lower panels) show negative values that were plotted at their absolute values to make them visible. The dashed vertical lines indicate the cutoff wavelength below which values of the CCD-SR were normally set to zero. Note the different spectral actinic flux density and wavelength ranges.

The overall performance of the CCD-SR was evaluated by a comparison of photolysis frequencies during the comparison periods. Figure 13 shows an example of correlation plots and ratios of photolysis frequencies as a function of solar zenith angles and the reference values for the most critical $j(O^1D)$. The scatter visible in the correlation plots is caused by the DM-SR scanning operation under variable atmospheric conditions, i.e. by the presence of moving clouds, in particular under broken-cloud

5 conditions. These variations can go in both directions and cancel each other out over longer periods, i.e. they do not influence the slope of linear regressions which are taken as a measure for the agreement of the measurements. Table 4 shows an overview of regression line slopes from all ground-based comparisons associated with various airborne deployments for $j(O^1D)$ and $j(NO_2)$. Including optical receiver corrections, deviations from unity are typically within $\pm 5\%$. The remaining discrepancies are attributed to uncertainties of the laboratory and in-field calibrations, optical receiver corrections and differences in spectral

10 resolutions.

No linearity problems are evident for CCD-SR or DM-SR measurements but the plots in Fig. 13 of $j(O^1D)$ ratios as a function of solar zenith angles and $j(O^1D)$ reveal increased scatter towards low sun or low $j(O^1D)$ when the detection limits of the instruments are approached. For comparison CCD-SR data are shown where spectral actinic flux densities below the cutoff wavelengths were set to zero (blue) and where this was not made (red). In the latter case scatter is apparently greater

15 because of higher CCD-SR detection limits in accordance with the results of Sect. 2.2.6. In fact, for the DM-SR nighttime $j(O^1D)$ standard deviations of $8\times10^{-9}s^{-1}$ were obtained while for instrument 62001 $2\times10^{-9}s^{-1}$ and $4\times10^{-8}s^{-1}$ resulted with and without setting flux densities to zero below cutoff wavelengths, respectively. The scatter of the red data points in Fig. 13 is therefore mainly caused by the detection limit of the CCD-SR while that of the blue points is dominated by the detection limit of the DM-SR. In any case, disregarding data below the cutoff wavelengths has virtually no effect for $j(O^1D)$ greater

20 than about $2\times10^{-7}s^{-1}$. Therefore this procedure is recommended but not crucial unless very small values of $j(O^1D)$ are of interest. The standard deviations mentioned above correspond to $j(O^1D)$ detection limits of about $6\times10^{-9}s^{-1}$ and $1\times10^{-7}s^{-1}$, corresponding to no more than around 0.02% and 0.4% of typical summer noontime values, respectively.

For $j(NO_2)$ nighttime standard deviations of $2.4\times10^{-8}s^{-1}$ and $1.6\times10^{-7}s^{-1}$ were obtained for the DM-SR and the CCD-SR 62001. For the CCD-SR the value is greater than predicted by considering dark noise alone (Tab. 3). This is attributed to the

25 fact that the determination of dark signals was optimized for the UV-B range and that for greater wavelengths the background is extrapolated. Improvements on the $j(NO_2)$ detection limits of the CCD-SR could probably be obtained by expanding the concept of cutoff wavelengths above 310 nm and for SZA>90°. On the other hand, there seems to be no need for such an improvement because values below the current detection limit of about $5\times10^{-7}s^{-1}$ are considered insignificant.

Apparently, the higher level of stray light of the CCD-SR compared to the DM-SR is no major obstacle to derive accurate

30 photolysis frequencies, including $j(O^1D)$, at least for the applied type of instrument. Jäkel et al. (2007) came to the same conclusion but their preferred method of stray light correction was slightly different for the UG5-filtered instrument. It was based on a stray light spectrum obtained with a calibration lamp and a 700 nm cutoff filter that for each spectrum was scaled for matching averages in the 270–290 nm range.
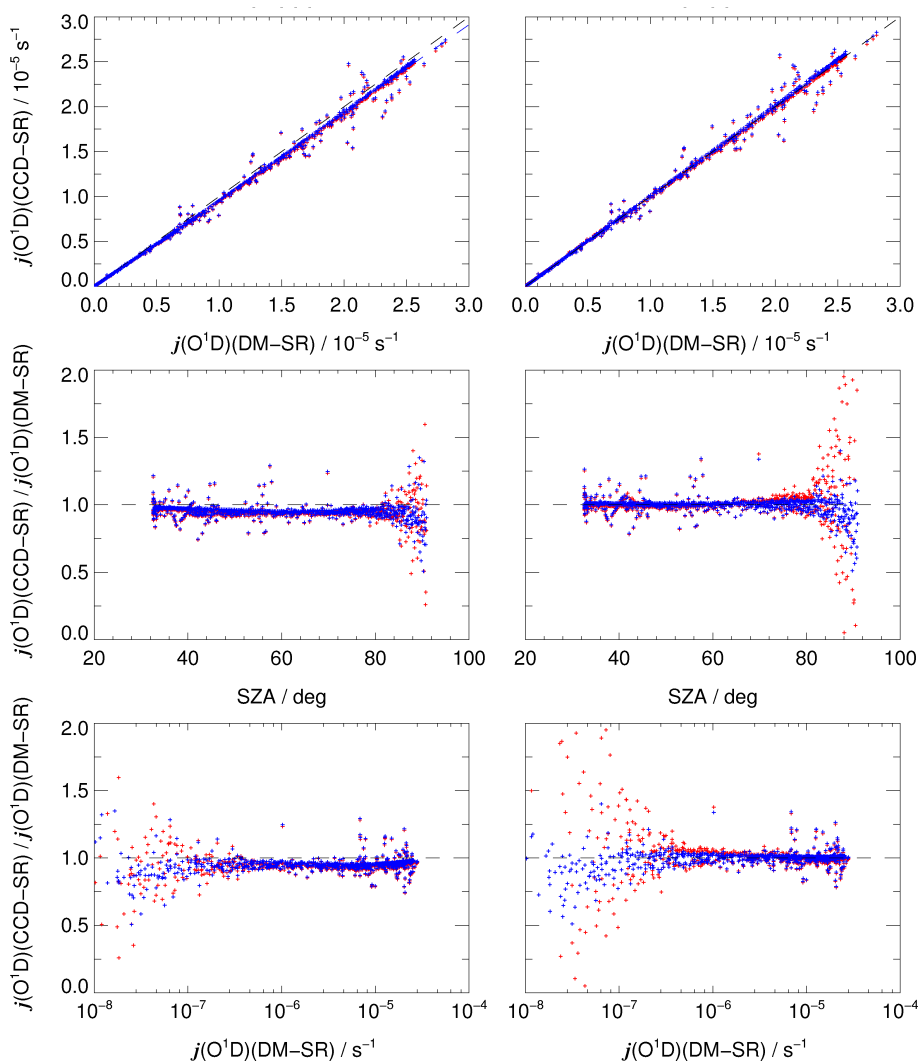
Figure 13. Comparisons of $j(O^1D)$ photolysis frequencies obtained on the ground with a double-monochromator based reference instrument (DM-SR) and instruments 62000 (left) and 62001 (right). Measurements were made during the period 30 Jul –01 Aug 2013 at Jülich (Germany). Dashed lines indicate 1:1 relationships. Scatter visible in the correlation plots (upper panels) is caused by clouds, i.e. by synchronisation issues. Additional scatter in the ratios towards large SZA (middle panels) and low $j(O^1D)$ (lower panels) is caused by different detection limits. Blue and red data points were obtained when spectral actinic flux densities below cutoff wavelengths were set to zero and not set to zero, respectively.

Table 4. Results of ground-based spectroradiometer comparisons associated with contemporary airborne instrument deployments of different CCD-SR. The numbers are slopes of $j(O^1D)$ and $j(NO_2)$ regression lines based on 2-5 day parallel measurements with a DM-SR reference.

deployment	instruments	slope (instrument vs. reference)	
	top / bottom	$j(O^1D)$	$j(NO_2)$
HALO 2010	62001 / 62000	1.003 / 0.997	0.956 / 0.972
Zeppelin 2012	45853 / 62001	1.034 / 1.054	0.998 / 0.979
Zeppelin 2013	62008 / 85235	1.001 / 1.035	0.978 / 0.981
HALO 2013	62001 / 62000	1.005 / 0.969	0.964 / 0.955
HALO 2015	62001 / 62000	1.019 / 0.959	0.981 / 0.957

More sophisticated stray light correction methods were developed in the past for array spectroradiometers using tunable light sources to investigate the instrument's stray light response as a function of wavelength. With this instrument-specific information, a correction can be made based on the measured spectra alone (Zong et al., 2006). However, for the instruments described in this work, a substantial fraction of the stray light comes from a spectral region beyond the measured range and this unaccounted fraction is strongly variable dependent on the presence or absence of direct sunlight. Because the same problem arises for atmospheric spectral irradiance measurements in the UV-B range, the method by Zong et al. (2006) was refined for these applications (Kreuter and Blumthaler, 2009; Nevas et al., 2014). However, a recent blind inter-comparison of spectral UV irradiance and UV-index measurements revealed that these methods are not consistently adhered to and accurate stray light corrections remain a complicated and critical issue (Egli et al., 2016).

3.3 Flight example

An example of photolysis frequencies obtained during a research flight with HALO is shown in Fig. 14 together with some flight related data. The route led from Oberpfaffenhofen in Germany to the island of Barbados in the Western Atlantic Ocean and was part of the NARVAL campaign conducted in December 2013 and January 2014 (Klepp et al., 2014). Flight altitudes were 12–14 km during the main part of the transfer with the aircraft presumably above any underlying clouds. The high altitude also resulted in low ambient temperatures around 210 K. Owing to the season and the times of day, solar zenith angles were changing in a narrow range of 55–75° even though the destination was at much lower latitudes. Also shown in Fig. 14 are the interpolated ozone columns along the flight track from satellite data that exhibit a typical decrease of ozone columns towards lower latitudes.

For the photolysis frequencies $j(O^1D)$ and $j(NO_2)$ the directly measured downward and upward components are shown in Fig. 14 as well as the photochemically relevant total values. Downward photolysis frequencies exhibit a smooth diurnal variation typical for cloud-free conditions above the aircraft. In contrast, upward photolysis frequencies show stronger, sometimes rapid fluctuations caused by underlying clouds. The contributions of upward radiation are comparable for $j(O^1D)$ and $j(NO_2)$

but differ in detail. Moreover, diurnal variations are strongly different for the two photolysis frequencies because of a more distinct dependency of $j(O^1D)$ on solar zenith angles. In addition $j(O^1D)$ was strongly influenced by total ozone columns which can be recognized in the first part of the flight.

The effect of ambient temperature is also more pronounced for $j(O^1D)$. Compared to a reference temperature of 298 K, in this example, $j(O^1D)$ and $j(NO_2)$ are smaller by factors of 0.73 and 0.92, respectively. These numbers are based on the temperature dependence of the molecular data from the literature (Daumont et al., 1992; Matsumi et al., 2002; Merienne et al., 1995; Troe, 2000) and demonstrate the importance of ambient temperature for aircraft measurements. A further analysis of spectral actinic flux densities or photolysis frequencies obtained during airborne missions is outside the focus of this work and will be given elsewhere.

4   Conclusions

Spectral actinic flux densities can be measured with high accuracy and high time resolution in the atmospherically relevant UV/VIS range using CCD array spectroradiometers. Because the instruments are compact and mechanically robust, they are suitable for high quality airborne measurements. In this work, we investigated the key properties of a widely used instrument type in the laboratory, developed a straightforward method for calibrations with irradiance standards, and derived a scheme to evaluate field measurements under variable atmospheric conditions. The major difficulties were accurate measurements in the UV-B range because calibrations and field measurements are affected by the notorious stray light problem which is typical for single-monochromator applications. We showed that this problem can be widely resolved in the laboratory by the use of long path cutoff filters including additional corrections, and during field measurements by utilizing the variable natural long path cutoff provided by the stratospheric ozone layer. Ground-based field comparisons with a double-monochromator reference instrument confirmed the practicality of the approach for atmospheric measurements. Even though the stray light effects do not completely vanish they can be contained so that they become insignificant for the determination of photolysis frequencies, including $j(O^1D)$. However, it should be noted that the results of this work refer to the radiometric part of the determination of photolysis frequencies. Additional uncertainties exist that are related with molecular parameters of photolyzed species. These uncertainties are process specific and are substantial for many photolysis processes mainly because quantum yields are poorly known. Because of extreme temperature conditions this problem should be kept in mind, in particular for airborne applications. Optical receiver issues are also more pronounced for airborne measurements but can be dealt with independently because they are not directly related with the type and performance of the spectroradiometer employed.

Acknowledgements. The authors thank a great number of people who helped to get instruments airborne on the platforms HALO and Zeppelin NT. We thank Bernhard Mayer, Arve Kylling and co-workers for making the libRadtran radiation transfer model available to the scientific community. Public provision of total ozone column data by the TEMIS/ESA team is gratefully acknowledged. We thank the Deutsche Forschungsgemeinschaft for funding under grant BO 1580/4-1.
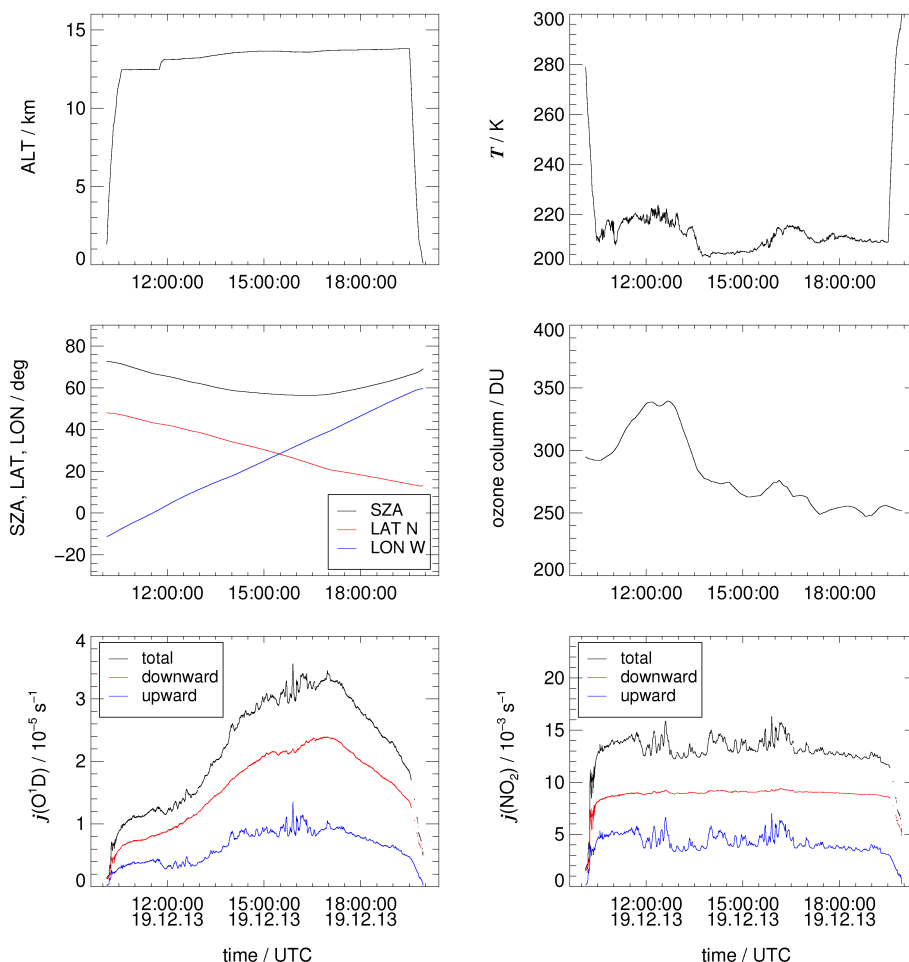
Figure 14. Example data from a HALO research flight on 19 Dec 2013 from Oberpfaffenhofen (Germany) to Barbados. Altitude (ALT), static temperature (T), location (LAT, LON), solar zenith angles (SZA) and total ozone columns are important boundary conditions and parameters used in the data evaluation. Photolysis frequencies $j(\text{O}^1\text{D})$ and $j(\text{NO}_2)$ were calculated for the corresponding static temperatures. Rapid fluctuations of upward components of photolysis frequencies were induced by underlying clouds.

References

Bohn, B., Corlett, G. K., Gillmann, M., Sanghavi, S., Stange, G., Tensing, E., Vrekoussis, M., Bloss, W. J., Clapp, L. J., Kortner, M., Dorn, H.-P., Monks, P. S., Platt, U., Plass-Dülmer, C., Mihalopoulos, N., Heard, D. E., Clemitshaw, K. C., Meixner, F. X., Prevot, A. S. H., and Schmitt, R.: Photolysis frequency measurement techniques: results of a comparison within the ACCENT project, Atmospheric Chemistry and Physics, 8, 5373–5391, doi:10.5194/acp-8-5373-2008, http://www.atmos-chem-phys.net/8/5373/2008/, 2008.

Daumont, D., Charbonnier, J. B. J., and Malicet, J.: Ozone UV spectroscopy I: Absorption cross-sections at room temperature, J. Atmos. Chem., 15, 145–155, 1992.

Eckstein, E., Perner, D., Brühl, C., and Trautmann, T.: A new actinic flux 4π-spectroradiometer: instrument design and application to clear sky and broken cloud conditions, Atmos. Chem. Phys., 3, 1965–1979, 2003.

Edwards, G. D. and Monks, P. S.: Performance of a single monochromator diode array spectroradiometer for the determination of actinic flux and atmospheric photolysis frequencies, J. Geophys. Res., 108, 8546, doi:10.1029/2002JD002844, 2003.

Egli, L., Gröbner, J., Hülsen, G., Bachmann, L., Blumthaler, M., Dubard, J., Khazova, M., Kift, R., Hoogendijk, K., Serrano, A., Smedley, A., and Vilaplana, J.-M.: Quality assessment of solar UV irradiance measured with array spectroradiometers, Atmospheric Measurement Techniques, 9, 1553–1567, doi:10.5194/amt-9-1553-2016, http://www.atmos-meas-tech.net/9/1553/2016/, 2016.

Emde, C., Buras-Schnell, R., Kylling, A., Mayer, B., Gasteiger, J., Hamann, U., Kylling, J., Richter, B., Pause, C., Dowling, T., and Bugliaro, L.: The libRadtran software package for radiative transfer calculations (version 2.0.1), Geoscientific Model Development, 9, 1647–1672, doi:10.5194/gmd-9-1647-2016, http://www.geosci-model-dev.net/9/1647/2016/, 2016.

Eskes, H. J., Velthoven, P. F. J. V., Valks, P. J. M., and Kelder, H. M.: Assimilation of GOME total-ozone satellite observations in a three-dimensional tracer-transport model, Quarterly Journal of the Royal Meteorological Society, 129, 1663–1681, doi:10.1256/qj.02.14, http://dx.doi.org/10.1256/qj.02.14, 2003.

Hofzumahaus, A.: Measurement of Photolysis Frequencies in the Atmosphere, in: Analytical Techniques for Atmospheric Measurement, D. E. Heard (Ed.), chap. 9, pp. 406–500, Blackwell Publishing, 2006.

Hofzumahaus, A., Kraus, A., and Müller, M.: Solar actinic flux spectroradiometry: A technique for measuring photolysis frequencies in the atmosphere, Applied Optics, 38, 4443–4460, 1999.

Hofzumahaus, A., Lefer, B. L., Monks, P. S., Hall, S. R., Kylling, A., Mayer, B., Shetter, R. E., Junkermann, W., Bais, A., Calvert, J. G., Cantrell, C. A., Madronich, S., Edwards, G. D., Kraus, A., Müller, M., Bohn, B., Schmitt, R., Johnston, P., McKenzie, R., Frost, G. J., Griffioen, E., Krol, M., Martin, T., Pfister, G., Röth, E. P., Ruggaber, A., Swartz, W. H., Lloyd, S. A., and VanWeele, M.: Photolysis frequency of O_3 to $O(^1D)$: Measurement and modelling during the international photolysis frequency measurement and modelling intercomparision (IPMMI), J. Geophys. Res., 109, D08S90, doi:10.1029/2003JD004333, 2004.

Jäkel, E., Wendisch, M., Kniffka, A., and Trautmann, T.: Airborne system for fast measurements of upwelling and downwelling spectral actinic flux densities, Applied Optics, 44, 434–444, 2005.

Jäkel, E., Wendisch, M., Blumthaler, M., Schmitt, R., and Webb, A. R.: A CCD spectroradiometer for ultraviolet actinic radiation measurements, J. Atmos. Ocean. Tech., 24, 449–462, doi:10.1175/JTECH1979.1, 2007.

Kanaya, Y., Kajii, Y., and Akimoto, H.: Solar actinic flux and photolysis frequency determinations by radiometers and a radiative transfer model at Rishiri Island: comparisons, cloud effects, and detection of an aerosol plume from Russian forest fires, Atmospheric Environment, 37, 2463–2475, 2003.

Klepp, C., Ament, F., Bakan, S., Hirsch, L., and Stevens, B.: NARVAL campaign report, vol. 164 of *Reports on Earth System Science, ISSN 1614-1199*, Max Planck Institute for Meteorology, Hamburg, 2014.

Kraus, A., Rohrer, F., and Hofzumahaus, A.: Intercomparison of NO_2 photolysis frequency measurements by actinic flux spectroradiometry and chemical actinometry during JCOM97, J. Geophys. Res. Lett., 27, 1115–1118, 2000.

5 Kreuter, A. and Blumthaler, M.: Stray light correction for solar measurements using array spectrometers, Review of Scientific Instruments, 80, doi:10.1063/1.3233897, 2009.

Lohse and Bohn: Optical receiver characterisations and corrections for airborne measurements of spectral actinic flux densities, manuscript in preparation, 2017.

Matsumi, Y., Comes, F. J., Hancock, G., Hofzumahaus, A., Hynes, A. J., Kawasaki, M., and Ravishankara, A. R.: Quantum yields for
10 production of $O(^1D)$ in the ultraviolet photolysis of ozone: Recommendation based on evaluation of laboratory data, J. Geophys. Res., 107, doi:10.1029/2001JD000510, 2002.

Mayer, B. and Kylling, A.: Technical note: The libRadtran software package for radiative transfer calculations - description and examples of use, Atmospheric Chemistry and Physics, 5, 1855–1877, doi:10.5194/acp-5-1855-2005, http://www.atmos-chem-phys.net/5/1855/2005/, 2005.

15 Merienne, M. F., Jenouvrier, A., and Coquart, B.: The NO_2 absorption spectrum: 1. Absorption cross-sections at ambient temperature in the 300 - 500 nm region, J. Atmos. Chem., 20, 281–297, 1995.

Nevas, S., Groebner, J., Egli, L., and Blumthaler, M.: Stray light correction of array spectroradiometers for solar UV measurements, Applied Optics, 53, 4313–4319, doi:10.1364/AO.53.004313, 2014.

Petropavlovskikh, I., Shetter, R., Hall, S., Ullmann, K., and Bhartia, P. K.: Algorithm for the charge-coupled-device scanning actinic flux
20 spectroradiometer ozone retrieval in support of the Aura satellite validation, Journal of Applied Remote Sensing, 1, 013 540–013 540–22, doi:10.1117/1.2802563, http://dx.doi.org/10.1117/1.2802563, 2007.

Sansonetti, C. J., Salit, M. L., and Reader, J.: Wavelengths of spectral lines in mercury pencil lamps, Appl. Opt., 35, 74–77, doi:10.1364/AO.35.000074, http://ao.osa.org/abstract.cfm?URI=ao-35-1-74, 1996.

Shetter, R. E. and Müller, M.: Photolysis frequency measurements using actinic flux spectroradiometry during PEM-Tropics Mission: Instru-
25 mentation description and some results, J. Geophys. Res., 104, 5647–5661, 1999.

Shetter, R. E., Junkermann, W., Swartz, W. H., Frost, G. J., Crawford, J. H., Lefer, B. L., Barrick, J. D., Hall, S. R., Hofzumahaus, A., Bais, A., Calvert, J. G., Cantrell, C. A., Madronich, S., Müller, M., Kraus, A., Monks, P. S., Edwards, G. D., McKenzie, R., Johnston, P., Schmitt, R., Griffioen, E., Krol, M., Kylling, A., Dickerson, R. R., Lloyd, S. A., Martin, T., Gardiner, B., Mayer, B., Pfister, G., Röth, E. P., Koepke, P., Ruggaber, A., Schwander, H., and van Weele, M.: Photolysis frequency of NO_2: Measurement and modelling during the international
30 photolysis frequency measurement and modelling intercomparision (IPMMI), J. Geophys. Res., 108, 8544, doi:10.1029/2002JD002932, 2003.

Stark, H., Lerner, B. M., Schmitt, R., Jakoubek, R., Williams, E. J., Ryerson, T. B., Sueper, D. T., Parrish, D. D., and Fehsenfeld, F. C.: Atmospheric in situ measurement of nitrate radical (NO_3) and other photolysis rates using spectroradiometry and filter radiometry, J. Geophys. Res., 112, D10S04, doi:10.1029/2006JD007578, 2007.

35 Troe, J.: Are primary quantum yields of NO_2 photolysis at $\lambda \leq 398$ nm smaller than unity?, Z. Phys. Chem., 214, 573–581, 2000.

Zong, Y., Brown, S., Johnson, B., Lykke, K., and Ohno, Y.: Simple spectral stray light correction method for array spectroradiometers, Applied Optics, 45, 1111–1119, doi:10.1364/AO.45.001111, 2006.